TU Delft

Delft University of Technology

Revisiting Active Manipulators in Aircraft Flight Control

Fu, Wei; van Paassen, Rene; Mulder, Max

DOI
10.2514/6.2019-1231

Publication date
2019

Document Version
Final published version

Published in
AIAA Scitech 2019 Forum

Citation (APA)
Fu, W., van Paassen, R., & Mulder, M. (2019). Revisiting Active Manipulators in Aircraft Flight Control. In *AIAA Scitech 2019 Forum: 7-11 January 2019, San Diego, California, USA* Article AIAA 2019-1231 https://doi.org/10.2514/6.2019-1231

Important note
To cite this publication, please use the final published version (if applicable).
Please check the document version above.

Copyright
Other than for strictly personal use, it is not permitted to download, forward or distribute the text or part of it, without the consent of the author(s) and/or copyright holder(s), unless the work is under an open content license such as Creative Commons.

Takedown policy
Please contact us and provide details if you believe this document breaches copyrights.
We will remove access to the work immediately and investigate your claim.

This work is downloaded from Delft University of Technology.
For technical reasons the number of authors shown on this cover page is limited to a maximum of 10.

AIAA SciTech Forum
7-11 January 2019, San Diego, California
AIAA Scitech 2019 Forum

10.2514/6.2019-1231

Check for updates

Revisiting Active Manipulators in Aircraft Flight Control

Wei Fu *, M. M. van Paassen† and Max Mulder‡
Delft University of Technology, Delft, the Netherlands, 2600 GB

This study revisits the active manipulator developed for manual aircraft control. The active manipulator sends the force applied by the pilot to the aircraft while feeding back the aircraft rotational velocity by means of its deflection angle. We find that the active manipulator, in comparison with the conventional passive manipulator, greatly facilitates target following and disturbance rejection in compensatory tasks. We also find that greater improvements in task performance are associated with higher forcing-function bandwidths. The findings are accounted for by the fact that the active manipulator changes the effective controlled element dynamics into an integrator, and integrates the disturbance rejection into the neuromuscular system. Furthermore, we demonstrate that the haptic feel of the active manipulator depends on the dynamics of the aircraft. With further exploration, we reveal that human haptic perception of the active manipulator could be characterized by mass-spring-damper properties.

Downloaded by TU DELFT on May 28, 2019 | http://arc.aiaa.org | DOI: 10.2514/6.2019-1231

Nomenclature

A	=	amplitude of the sinusoidal component of the forcing function, [rad]
b_{pm}	=	damping constant of the passive manipulator, [Nms/rad]
e	=	tracking error, [deg]
f_d	=	disturbance forcing function, [rad]
f_d^*	=	adapted disturbance forcing function, [rad]
f_m	=	pilot's force, [N·m]
f_t	=	target forcing function, [rad]
G_{ds}	=	human perceived dynamics of a dynamic system
G_m	=	human perceived dynamics of the active manipulator
G_{msd}	=	human perceived dynamics of a mass-spring-damper system
H_{am}	=	dynamics of the active manipulator
H_c	=	dynamics of the controlled element
$H_{c,eff}$	=	effective dynamics of the controlled element for the active manipulator
H_{CL}	=	closed-loop dynamics of the overall system
H_e	=	dynamics of the pilot's response to the visual error
H_{pm}	=	dynamics of the passive manipulator
H_{OL}	=	open-loop dynamics of the overall system
H_x	=	dynamics of the pilot's response to the manipulator movement
K_c	=	controlled element gain
K_f	=	forward gain of the aircraft control loop
K_m	=	gain of the servo system of the active manipulator
k_{pm}	=	spring constant of the passive manipulator, [Nm/rad]
m_{pm}	=	inertia constant of the passive manipulator, [kgm^2]
s	=	Laplace variable
u_p	=	pilot control signal
x_m	=	manipulator deflection angle, [rad]
ϕ	=	roll angle, [rad]
$\dot{\phi}$	=	roll rate, [rad/s]
ϕ_m	=	phase margin, [deg]
ω	=	frequency, [rad/s]

*PhD student, section Control and Simulation, Faculty of Aerospace Engineering, w.fu-1@tudelft.nl, Student Member AIAA.
†Associate professor, section Control and Simulation, Faculty of Aerospace Engineering, m.m.vanpaassen@tudelft.nl, Member AIAA.
‡Full professor, section Control and Simulation, Faculty of Aerospace Engineering, m.mulder@tudelft.nl, AIAA Associate Fellow.

Copyright © 2019 by Delft University of Technology. Published by the American Institute of Aeronautics and Astronautics, Inc., with permission.

ω_c = crossover frequency, [rad/s]

Subscripts

d = disturbance rejection
t = target following

I. Introduction

In recent years, the haptic interface has received increased interest and facilitated manual control task innovations in many fields, such as surgical robots, terrestrial and space operations and nuclear plant operations [1–5]. In general, a haptic interface is established with a control manipulator, from which the human operator exerts control while haptically receiving information about the controlled system.

In contrast to conventional aircraft controls, where the pilot controls the aircraft through a passive manipulator and only receives information about the aircraft state through the vision and motion sensory systems, the haptic interface introduces additional ways to inform the pilot. The fly-by-wire system of modern aircraft offers the possibility to design the control manipulator as a haptic interface, thereby establishing bilateral transmission of information and facilitating manual aircraft control. In general, existing haptic interfaces developed for aircraft control work as support systems which inform the pilot about one or more aspects, such as the current flight condition, the task, or constraints (e.g., boundaries, dangers) in the environment. The common approach taken is by providing additional forces commanded by a haptic support system [6, 7]. However, the manipulator itself is still a passive device with its own dynamics, decoupled from those of the aircraft. Due to this, a direct connection between the pilot and the aircraft is not fully established.

Apart from the haptic support system, there is still much room for improvement on the manipulator itself. To this end, in this study we fundamentally change the nature of the manipulator. The current work draws primarily on the foundation laid by previous attempts by Hosman et al. [8, 9] in which the active manipulator was developed. The active manipulator is based on the admittance display architecture [10], in which the state of the controlled aircraft is displayed through the movement of the control manipulator. The pilot's control input to the aircraft, in this case, is derived from the force applied to the manipulator (see Section II for more details). In this way, the manipulator is completely coupled to the aircraft.

It was demonstrated that the prototype of the active manipulator led to considerable improvements in the flight-control performance [8, 9]. However, knowledge about the guiding principle that accounts for such improvements is still lacking. Moreover, attempts at further development of the active manipulator were impeded at that time by the rather limited knowledge of human haptic perception.

In this study an investigation was conducted firstly, to allow for corroboration of the previous findings, and to gather theoretical evidence that supports those findings. To this end, an experiment in which participants performed compensatory tasks with various forcing-function bandwidths was carried out. Secondly, using recent understandings established on human haptic perception [11–17], we further explored the characteristics of the haptic perception of the manipulator dynamics.

This paper is organized as follows: In the next section, the design principle behind the active manipulator is elaborated. The set-up of the first experiment drawing comparisons between the active and passive manipulators, and the corresponding result along with the analysis are then given in Sections III and IV, respectively. The principle behind the pilot's performance improvement associated with the active manipulator is revealed in Section V. In Section VI, the active manipulator is further evaluated in terms of what it would be perceived as. The contributions of this study are discussed and summarized in Sections VII and VIII.

II. Active manipulator

In conventional aircraft control that employs a passive manipulator, the pilot only receives information about the aircraft state through vision and motion. Different from the passive manipulator, the active manipulator allows the pilot to directly perceive an aircraft output, typically the aircraft rotational velocity, through the manipulator. For instance, consider the control of the aircraft roll angle, as can be seen in Fig. 1.

Downloaded by TU DELFT on May 28, 2019 | http://arc.aiaa.org | DOI: 10.2514/6.2019-1231

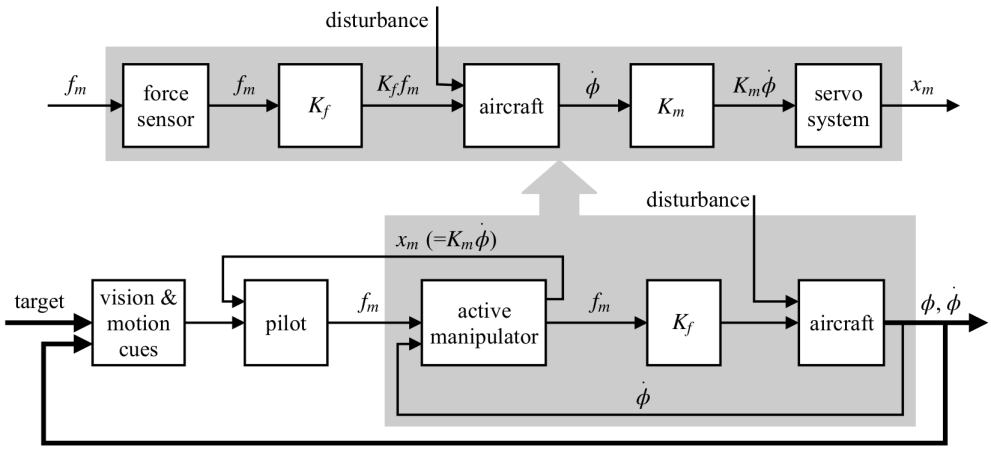

Fig. 1 Schematic diagram of the control of the aircraft roll attitude with the active manipulator.

Downloaded by TU DELFT on May 28, 2019 | http://arc.aiaa.org | DOI: 10.2514/6.2019-1231

In addition to other sensory channels, the active manipulator involves the haptic channel in perceiving the state of the aircraft. In conventional aircraft control, the deflection of the passive manipulator is fed to the aircraft. In the case of the active manipulator, however, the force f_m that the pilot applies on the manipulator is used as the command. The manipulator no longer behaves like a passive manipulator, instead, its deflection is driven by a position servo system which tracks the angular velocity of the aircraft, $\dot{\phi}$. If we ignore the dynamics of the force sensor and servo system, the deflection of the active manipulator x_m is proportional to $\dot{\phi}$: $x_m = K_m\dot{\phi}$.

As compared to the passive manipulator, the active manipulator leads to significant improvement in the flight-control performance [8, 9]. However, as mentioned earlier, such findings still lack a theoretical basis. In order to obtain more insights, and to provide a comparison with the previous results, an experiment is designed in the following section.

III. Experiment one

A roll-axis compensatory task, which involves both target following and disturbance rejection, is performed. The two manipulator types, namely the active and passive manipulator, are compared in terms of the task performance. The target and disturbance signals are designed with three different bandwidths to evaluate the active manipulator in cases of different task difficulties. The remainder of this section gives details about the experiment.

A. Setup of the compensatory task

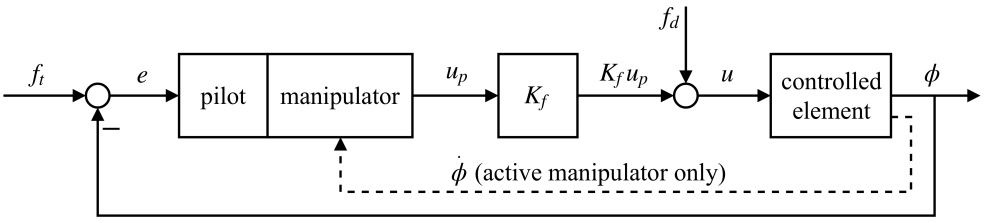

Fig. 2 Schematic diagram of the compensatory task.

Fig. 2 illustrates the compensatory task performed by a human pilot. As can be seen, the task requires the pilot to minimize the tracking error e, which is the difference between the target forcing function f_t and the output of the controlled element ϕ: $e = f_t - \phi$. In the experiment, e is presented on the visual display with a simplified artificial horizon indicator, as can be seen from Fig. 3.

The pilot generates the control signal u_p using the manipulator, on the basis of the visually perceived e. Here, for the passive manipulator, u_p is the manipulator deflection angle: $u_p = x_m$; for the active manipulator, u_p is the force

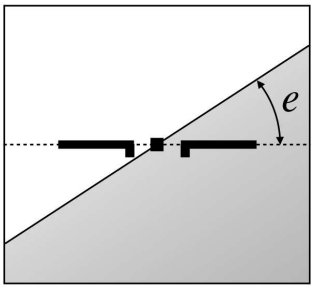

Fig. 3 Simplified artificial horizon.

that the pilot applies on the manipulator: $u_p = f_m$. The setups of the two manipulator types will be given later in greater detail. The forward gain K_f is set to 1 for both manipulator types. The input to the controlled element H_c is the combination of the control signal u_p and the disturbance forcing function f_d.

1. Controlled element

The roll dynamics of a typical wide-body jet aircraft [18] are used as the dynamics of the controlled element in the experiment. The spiral mode is simplified to a single integrator. The roll subsidence and the open-loop gain are deliberately adjusted in order to make the aircraft not too difficult to control.

$$H_c(s) = \frac{\Phi(s)}{U(s)} = \underbrace{\frac{1}{0.083s+1}}_{\text{actuator dynamics}} \cdot \underbrace{K_c \cdot \frac{2.259s^2 + 0.821s + 1}{s(0.4s+1)(1.647s^2 + 0.336s + 1)}}_{\text{aileron-to-roll-angle dynamics}} \tag{1}$$

Here the open-loop gain is $K_c = 3.5$.

2. Manipulator setup

When the passive manipulator is employed, the control signal u_p equals the manipulator deflection x_m. The passive manipulator used in this study resembles a mass-spring-damper system, the dynamics of which are:

$$H_{pm}(s) = \frac{X_m(s)}{F_m(s)} = \frac{1}{m_{pm}s^2 + b_{pm}s + k_{pm}} \tag{2}$$

Changing the deflection angle of the manipulator resembles moving a mass that is connected with a spring and a damper to an infinitely stiff basis. Table 1 lists the mass, damping and stiffness properties of the passive manipulator. Please note that all the mechanical properties are expressed in the rotational coordinate system, the corresponding linear values can be derived using the distance from the effective grip point to the axis of rotation (90 mm, see Section III.B for more details).

Table 1 Dynamic properties of the passive manipulator

m_{pm} [kgm^2]	b_{pm} [Nms/rad]	k_{pm} [Nm/rad]
0.012	0.2	2.0

In the case of the active manipulator, the control signal u_p equals the force f_m that the pilot applies on the manipulator. As mentioned earlier, the manipulator deflection x_m is proportional to the aircraft rotational velocity ($x_m = K_m\dot{\phi}$). However, the maximum $\dot{\phi}$ is limited by the maximum excursion of the manipulator. In order to obtain the same static gain of the controlled element as the passive manipulator, the gain of the servo system K_m (see Fig. 1) is set as the inverse of the aircraft static gain:

$$x_m = K_m \cdot \dot{\phi} = \frac{1}{K_c} \cdot \dot{\phi} \tag{3}$$

Downloaded by TU DELFT on May 28, 2019 | http://arc.aiaa.org | DOI: 10.2514/6.2019-1231

3. Duration

An experimental run lasts 90 seconds, during which the subject performs the compensatory task and the data are recorded. The first 8.08 seconds are used as the run-in time, to allow the subject to adjust to the task. The remaining 81.92 seconds yield the measurement data. In the experiment, each subject repeated the experimental run of each condition for a number of times. The number of repetitions varied from 8 to 10, depending on how rapidly the performance converged to a stable level. The last five repetitions were used as the measurement.

4. Forcing function and experimental condition

The two forcing functions f_t and f_d are both defined as the sum of ten different sinusoids [19]:

$$f_t(t) = \sum_{k=1}^{10} A_t(k) \cdot \sin(\omega_t(k)t + \theta_t(k)) \tag{4}$$

$$f_d(t) = \sum_{k=1}^{10} A_d(k) \cdot \sin(\omega_d(k)t + \theta_d(k)) \tag{5}$$

Using the two forcing functions, both the pilot's reaction to the visual presentation and the response to the manipulator movement, and thus the neuromuscular impedance during the task, can be estimated [20]. To prevent participants from recognizing the signal pattern, the starting phases of the sine components are chosen randomly, making the two signals appear random.

A lead-lag low-pass filter is selected to define the amplitudes of the forcing functions:

$$H_{ff} = K_{ff} \cdot \frac{\frac{1}{\omega_{ff,L}^2}s^2 + \frac{2\cdot\xi_{ff}}{\omega_{ff,L}}s + 1}{\frac{1}{\omega_{ff,l}^2}s^2 + \frac{2\cdot\xi_{ff}}{\omega_{ff,l}}s + 1}, \tag{6}$$

where the gain K_{ff} and the damping ratio ξ_{ff} are 0.2 and 0.7, respectively. The amplitude of each sinusoidal component of the forcing functions is given by the magnitude of the filter at the corresponding frequency. To obtain three different forcing-function bandwidths, the two corner frequencies are adjusted, as listed in Table 2.

Table 2 The corner frequencies of the magnitudes of the forcing functions

Bandwidth	$\omega_{ff,l}$ [rad/s]	$\omega_{ff,L}$ [rad/s]
BW1	0.60	4.80
BW2	1.00	8.00
BW2	1.65	13.2

To keep the target-following task and the disturbance-rejection task equal in difficulty, the disturbance forcing function is adapted by scaling its magnitude with the inverse of $|H_c|$, as illustrated by Fig. 4.

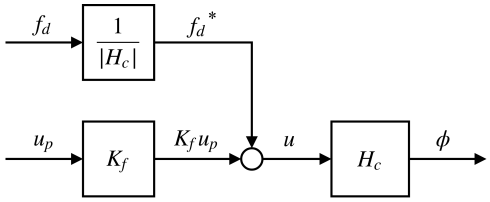

Fig. 4 The pre-filtering of the disturbance forcing function.

A factorial combination of the two manipulator types and the three forcing-function bandwidths yields six experimental conditions. Details about the definition of the two forcing functions are given in Tables 3 and 4, respectively.

Downloaded by TU DELFT on May 28, 2019 | http://arc.aiaa.org | DOI: 10.2514/6.2019-1231

Table 3 Target forcing function f_t

k	period	ω_t, [rad/s]	A_t, [rad]			ϕ_t, [rad]		
			BW1	BW2	BW3	BW1	BW2	BW3
1	5	0.3835	0.1864	0.1984	0.1999	1.7411	2.3319	4.9089
2	11	0.8437	0.0910	0.1645	0.1944	5.4434	5.5352	0.9319
3	21	1.6107	0.0277	0.0724	0.1462	3.3194	0.6807	5.0653
4	37	2.8379	0.0094	0.0248	0.0645	3.8945	5.8910	0.4305
5	51	3.9117	0.0056	0.0134	0.0352	1.2212	3.2216	1.8187
6	71	5.4456	0.0039	0.0074	0.0185	4.3954	0.9325	5.9087
7	101	7.7466	0.0033	0.0045	0.0095	3.0397	5.6708	4.8104
8	137	10.5078	0.0032	0.0036	0.0058	0.0160	1.1480	1.8858
9	191	14.6495	0.0031	0.0032	0.0040	5.4767	4.4054	2.0951
10	224	17.1806	0.0031	0.0032	0.0036	3.4525	4.0862	1.6544

Table 4 Adapted disturbance forcing function f_d^*

k	period	ω_d, [rad/s]	A_d, [rad]			ϕ_d, [rad]		
			BW1	BW2	BW3	BW1	BW2	BW3
1	6	0.4602	0.0242	0.0273	0.0278	1.2829	5.1081	0.4333
2	13	0.9971	0.0102	0.0213	0.0281	0.9194	4.1567	3.1062
3	23	1.7641	0.0097	0.0258	0.0557	1.8334	3.8964	0.1702
4	38	2.9146	0.0084	0.0220	0.0574	2.5865	1.1398	3.9334
5	53	4.0650	0.0090	0.0209	0.0551	1.5750	3.2806	1.2733
6	73	5.5990	0.0120	0.0221	0.0550	3.7298	3.5648	3.7481
7	103	7.9000	0.0215	0.0289	0.0599	1.5056	1.8805	3.0091
8	139	10.6612	0.0413	0.0462	0.0736	3.1201	1.6206	1.5561
9	194	14.8796	0.0934	0.0964	0.1173	1.0491	2.2507	1.9728
10	227	17.4107	0.1407	0.1430	0.1606	4.8887	4.3722	5.5454

Downloaded by TU DELFT on May 28, 2019 | http://arc.aiaa.org | DOI: 10.2514/6.2019-1231

B. Participants and Apparatus

Twelve subjects participated in the experiment. To ensure stable performance, extensive training was performed before the measurements were collected.

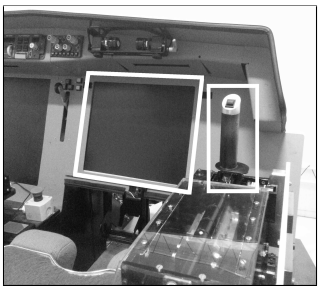

Fig. 5 Devices used for the experiment.

The visual display (an LCD screen) and the manipulator used for the experiment are marked by white boxes in Fig. 5. The manipulator is supplied with a handle, diameter 35 mm, with grooves for placement of the fingers. When

a hand is correctly placed on the handle, the center of the hand lies 90 mm above the manipulator rotation axis. The manipulator is equipped with a force sensor, and is driven by an electro-hydraulic position servo system of which the bandwidth is around 40 Hz. During the experiment, the manipulator movement around the pitch axis is fixed at the neutral position. The range of travel with respect to the roll axis is limited to ±0.47 [rad].

IV. Result and analysis

This section gives the result of the experiment. The measurements of the last five repetitions performed by each subject are averaged for the analysis. Comparisons between the two manipulator types are made in terms of the tracking error and the control effort, as well as the estimated open- and closed-loop frequency response functions.

A. Tracking error and control activity

1. Tracking Error

Fig. 6a shows the root mean square (RMS) of the error variable e. The symbols (triangles and squares) represent the average over all subjects. The variance bars indicate the 95% confidence interval corrected for between-subject variability.

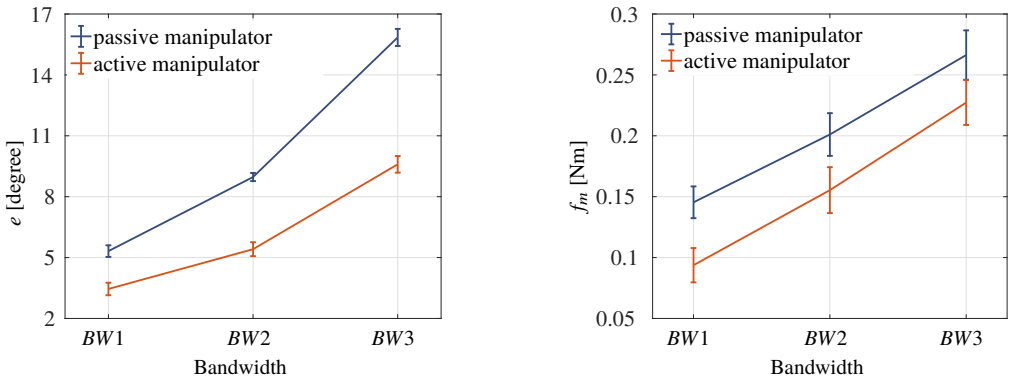

(a) RMS of e (b) RMS of f_m

Fig. 6 RMS of the error and force signals for different conditions.

As can be seen, the active manipulator leads to remarkably better performance. A two-way repeated measures analysis of variance (ANOVA) reveals significant effects of both the manipulator type and the forcing function bandwidth on the error signal e: $F(1, 11) = 655.2$, $p < 0.05$ for the manipulator type and $F(1.157, 12.728) = 867.9$, $p < 0.05$ (Greenhouse-Geisser correction) for the bandwidth. However, a significant interaction is also found ($F(2, 22) = 215.9$, $p < 0.05$). It can be readily seen from Fig. 6a that a much larger improvement in performance is obtained when the forcing-function bandwidth is higher.

2. Control activity

The control signals corresponding to the two manipulator types are f_m (active manipulator) and x_m (passive manipulator), respectively. Direct comparison between these two different variables may be misleading. Therefore, the control activities are evaluated on the basis of the force signals f_m, as can be seen from Fig. 6b. Compared to the passive manipulator, the active manipulator leads to significant reduction in the exerted forces ($F(1, 11) = 27.72$, $p < 0.05$). The forces for both manipulator types increases significantly as a result of the extended forcing-function bandwidth ($F(2, 22) = 103.4$, $p < 0.05$). This effect is independent of the manipulator type, as no interactions are found, $F(2, 22) = 0.405$, $p > 0.05$.

Downloaded by TU DELFT on May 28, 2019 | http://arc.aiaa.org | DOI: 10.2514/6.2019-1231

B. Frequency-domain analysis

1. Power spectrum of the tracking error

The power spectrum of the error e, corresponding to the forcing function BW2, measured for one subject is shown in Fig. 7. Similar characteristics are observed for all other bandwidths and subjects. In the case of the passive manipulator, the magnitudes of e at the frequencies of the target and the disturbance are similar. As for the active manipulator, the magnitudes that correspond to the frequencies of the target remain at roughly the same level as the passive manipulator. However, at the low frequency region, those related to the disturbance are considerably attenuated. This demonstrates an apparent advantage of active manipulator in rejecting the low-frequency disturbance. Moreover, the different extent to which the error is attenuated with the active manipulator also indicates that the two tasks are accomplished with different mechanisms.

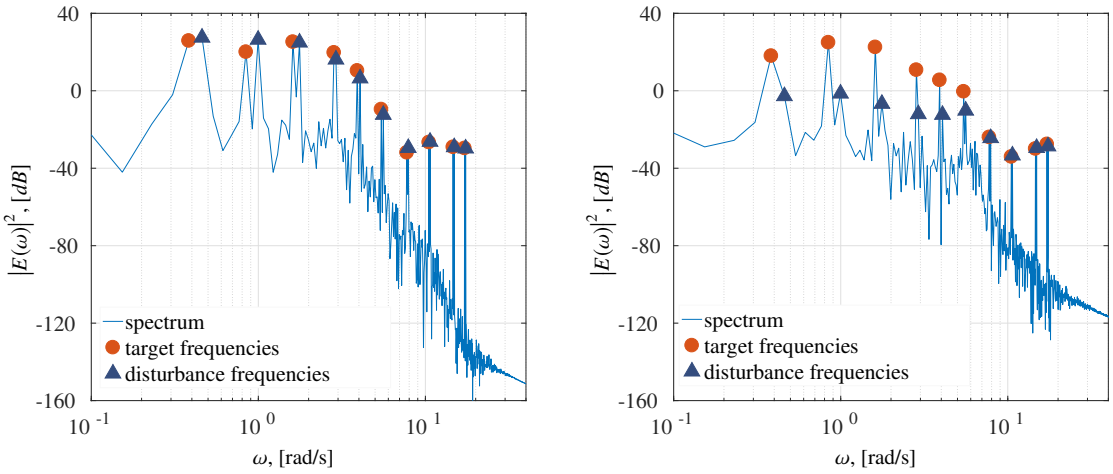

(a) Passive manipulator

(b) Active manipulator

Fig. 7 Power spectra of the error $e(t)$ (one subject, BW2).

2. Open- and closed-loop responses

The open- and closed-loop responses are investigated. Due to the fact that the active manipulator causes different power spectra of e at the frequencies of the target and the disturbance, the frequency responses for the two tasks are estimated separately. The open-loop frequency response of target following is obtained from the relation between e and ϕ at the frequencies of f_t:

$$H_{OL,t}(j\omega) = \frac{\Phi_t(j\omega)}{E_t(j\omega)}\,, \tag{7}$$

where $E(j\omega)$ and $\Phi(j\omega)$ denote the Fourier Transforms of the time-domain signals e and ϕ, respectively. The target-following close-loop response is obtained by:

$$H_{CL,t}(j\omega) = \frac{\Phi_t(j\omega)}{F_t(j\omega)} \tag{8}$$

Fig. 8 shows the average of the open- and closed-loop responses generated by subjects for the forcing function BW2. Similar characteristics of the responses can be observed for the other bandwidths. In the crossover region the magnitudes of the open-loop responses are similar for both manipulators and resemble those of a single integrator, as expected by McRuer's crossover model [21]. The active manipulator leads to a smaller phase lag and a greater phase margin. This leads to a larger bandwidth, less overshoots, and smaller phase lags in the closed-loop response, as compared to the passive manipulator.

The crossover frequencies ω_c and the phase margins ϕ_m of the open-loop responses averaged over all subjects are shown in Fig. 9, where the symbols and variance bars respectively indicate the average and ±95% confidence interval corrected for between-subject variability.

Downloaded by TU DELFT on May 28, 2019 | http://arc.aiaa.org | DOI: 10.2514/6.2019-1231

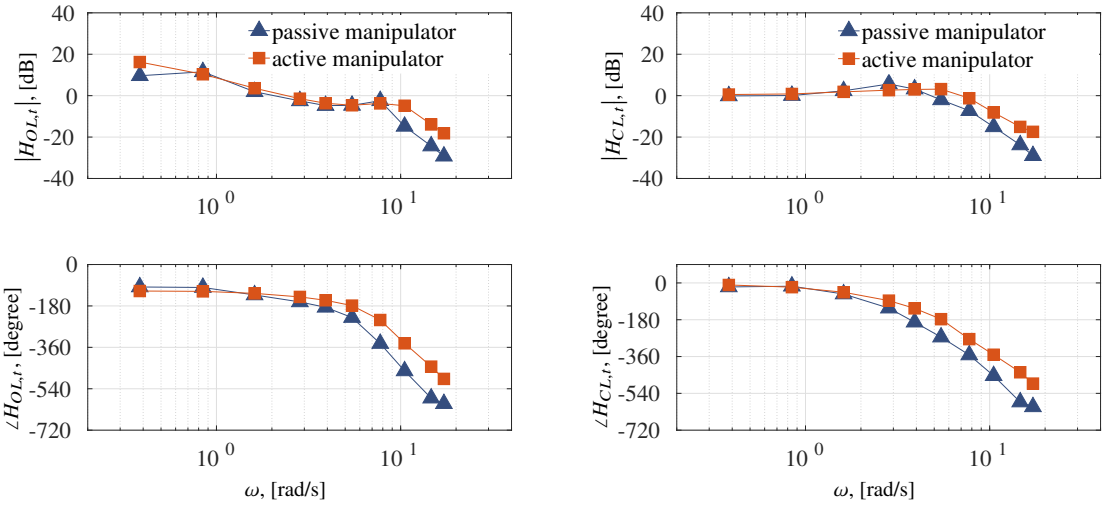

(a) Open loop response

(b) Closed loop response

Fig. 8 Target following frequency responses, BW2

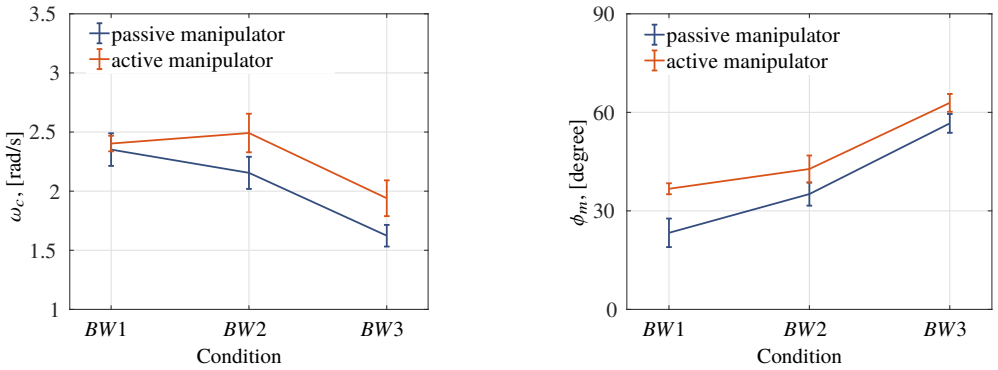

(a) Crossover frequency ω_c

(b) Phase margin ϕ_m

Fig. 9 Crossover frequencies and phase margins of target-following open-loop response.

Results from a two-way repeated measures ANOVA suggest that the effect of the manipulator type on ω_c is significant ($F(1, 11) = 13.63$, $p < 0.05$). Except for the lowest forcing-function bandwidth, the active manipulator leads to higher ω_c than the passive manipulator. The effect of the forcing-function bandwidth is also significant ($F(2, 22) = 66.43$, $p < 0.05$). For the active manipulator, ω_c remains at roughly the same level for the fist two forcing-function bandwidths, and then regresses for the highest bandwidth. For the passive manipulator, a regressing trend can be easily seen.

Significant effects of both the manipulator type and forcing-function bandwidth on ϕ_m are revealed ($F(1, 11) = 44.27$, $p < 0.05$ for the manipulator type and $F(2, 22) = 152.9$, $p < 0.05$ for the bandwidth). The active manipulator leads to a significantly higher ϕ_m than the passive manipulator for all three bandwidths. Also, for the active manipulator, ϕ_m remains roughly the same for the first two forcing function bandwidths. For the highest bandwidth, subjects regressed their ω_c to increase their ϕ_m and maintain stability of the closed-loop system. The ϕ_m corresponding to the passive manipulator increases as the forcing-function bandwidth increases, as a result of crossover regression.

The open-loop frequency response of disturbance rejection is derived through:

$$H_{OL,d}(j\omega) = \frac{U_{p,d}(j\omega)}{U_d(j\omega)}, \tag{9}$$

Downloaded by TU DELFT on May 28, 2019 | http://arc.aiaa.org | DOI: 10.2514/6.2019-1231

where $U_p = F_m$ in the case of the active manipulator and $U_p = X_m$ in the case of the passive manipulator. Since the disturbance is fed into the system before the controlled element (see Fig. 4), selecting f_d^* as the input to the closed-loop system will include the aircraft dynamics in the numerator. This will make the information provided by the closed-loop response not straightforward. Therefore, the following correction is made:

$$\begin{aligned} \left|H_{CL,d}(j\omega)\right| &= \left|\frac{\Phi_d(j\omega)}{F_d^*(j\omega)} / H_c(j\omega)\right| = \left|\frac{\Phi_d(j\omega)}{F_d(j\omega)}\right| \\ \angle H_{CL,d}(j\omega) &= \angle\frac{\Phi_d(j\omega)}{F_d^*(j\omega)} - \angle H_c(j\omega) \end{aligned} \tag{10}$$

This results in the frequency response of a closed-loop system into which the disturbance is fed directly at the output of the controlled element.

Fig. 10 shows the average of the open- and closed-loop frequency response estimates for all subjects, for the BW2 condition. The characteristics of the frequency responses estimated for the other two bandwidths are similar.

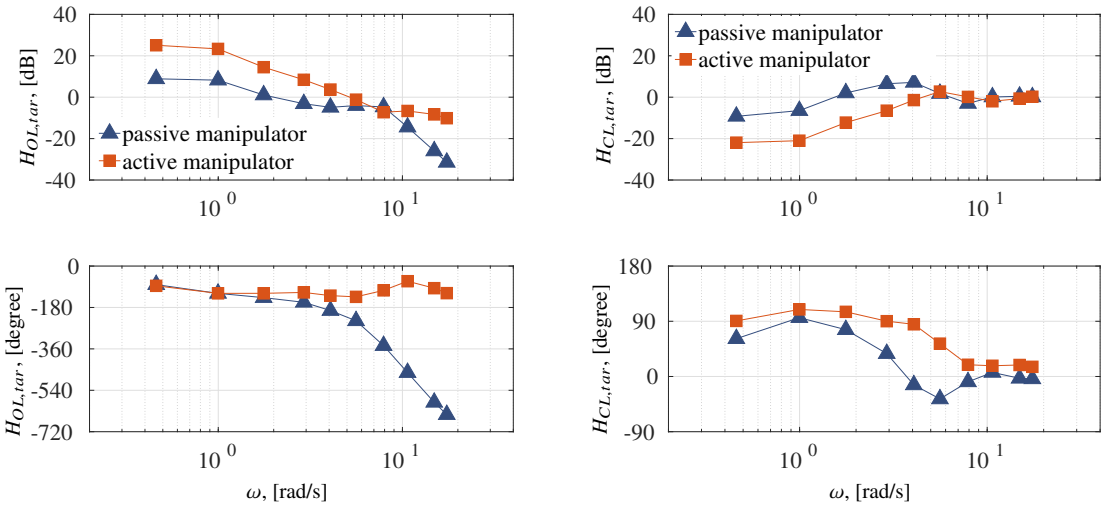

(a) Open loop response

(b) Closed loop response

Fig. 10 Disturbance rejection frequency responses, BW2

As can be seen, different manipulator types lead to notable differences in the frequency responses. These differences are much larger than those corresponding to target following. This is in line with that observed from the power spectrum of the error signal (see Fig. 7). The active manipulator leads to a larger open-loop gain in the crossover region. Moreover, the open-loop phase lag corresponding to the active manipulator is much smaller and remains at approximately -90 degrees over the whole tested range of frequency. Therefore, the closed-loop system demonstrates significant improvement in the rejection bandwidth and produces smaller overshoots, as can be seen from Fig. 10b.

The crossover frequencies ω_c and the phase margins ϕ_m of the open-loop responses generated by all subjects are shown in Fig. 11, where the symbols and variance bars respectively indicate the mean and ±95% confidence interval corrected for between-subject variability.

A two-way repeated measures ANOVA shows that the effects of both the manipulator type ($F(1, 11) = 298.6$, $p < 0.05$) and the forcing-functions bandwidth ($F(2, 22) = 4.987$, $p < 0.05$) on ω_c are significant. The interaction between these two factors is also significant ($F(2, 22) = 43.76$, $p < 0.05$), which can be expected since the two manipulator types lead to opposite effects of the forcing-function bandwidth on ω_c. For the passive manipulator, apparent crossover regression occurs. This is similar to the case of target following where a declining trend of ω_c is also observed, see Fig. 9. In contrast, ω_c for the active manipulator demonstrates a notable increasing trend as the bandwidth increases.

The active manipulator allows for significantly higher phase margins ($F(1, 11) = 14.49$, $p < 0.05$). As a result of crossover regression, the ϕ_m corresponding to the passive manipulator increases as the bandwidth increases. Due to

Downloaded by TU DELFT on May 28, 2019 | http://arc.aiaa.org | DOI: 10.2514/6.2019-1231

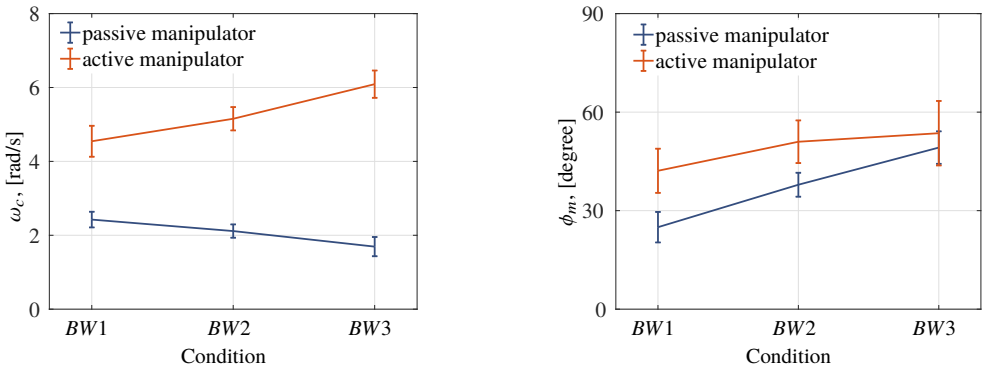

(a) Crossover frequency ω_c

(b) Phase margin ϕ_m

Fig. 11 Crossover frequencies and phase margins for disturbance-rejection open-loop response.

Downloaded by TU DELFT on May 28, 2019 | http://arc.aiaa.org | DOI: 10.2514/6.2019-1231

this, a significant effect of the forcing-function bandwidth is also revealed ($F(2, 22) = 17.38$, $p < 0.05$). In contrast, the ϕ_m with regard to the active manipulator remained roughly independent of the forcing-function bandwidth.

C. Discussion

With the passive manipulator, subjects generated similar open-loop responses for the target-following and disturbance-rejection tasks. The crossover frequencies ω_c and the phase margins ϕ_m corresponding to these two tasks, as well as the the effects of the forcing-function bandwidth, are similar. This is expected, as our subjects received the information of both the target and the disturbance *only* through the error presented visually. The frequency responses with respect to these two tasks, therefore, must be similar.

In general, the active manipulator leads to a pronounced performance improvement. An interesting fact associated with the active manipulator is that a clear distinction exists in the open-loop frequency response between target following and disturbance rejection, as well as in the characteristics of ω_c and ϕ_m. The disturbance rejection is associated with higher open-loop gains and smaller phase lags than the target following. Moreover, crossover regression occurs in target following in the case of the highest forcing-function bandwidth. However, ω_c of the disturbance rejection does not regress, instead, it *increases* when the forcing-function bandwidth increases.

This remarkable difference indicates that with the active manipulator, following the target and rejecting the disturbance were accomplished independently, although these two tasks were performed simultaneously. This maybe due to the fact that subjects benefited from the haptic feedback of the aircraft rotational velocity. The neuromuscular system which controls the movement of the manipulator may play a more important role in controlling the aircraft state. This hypothesis will be further explored in the following section.

V. Mechanism of aircraft control with the active manipulator

The mechanism of controlling the aircraft with the active manipulator can be presented more intuitively by means of a two-port network representation [22, 23], as can be seen in Fig. 12. Please note that the disturbance f_d and the forward gain K_f are omitted for the reason of simplicity. In addition, the arrow under $K_m\dot{\phi}$ indicates the direction of the energy flow, which is not necessarily the direction of the transmission of $\dot{\phi}$ [23].

We assume that the sampling and the servo system have negligible effects on the overall dynamics in the frequency range of interest. In this case, the force sensor and the servo system act as transparent mediums that directly connect the pilot to the aircraft. When the pilot applies a force on the manipulator, a change occurs in the aircraft rotational velocity. The manipulator moves at the same moment, as if it is moved by the pilot directly. In other words, when the pilot moves the manipulator, the rotational velocity of the aircraft exhibits exactly the same changes. One can imagine that the pilot still controls the aircraft attitude by means of the manipulator deflection, as he/she does with the passive manipulator. The dynamics of the manipulator *become* the dynamics that correspond to the aircraft rotational velocity in response to the aircraft input:

$$H_{am} = \frac{X_m(s)}{F_m(s)} = \frac{K_m \cdot s\Phi(s)}{U(s)} = K_m \cdot sH_c(s) \tag{11}$$

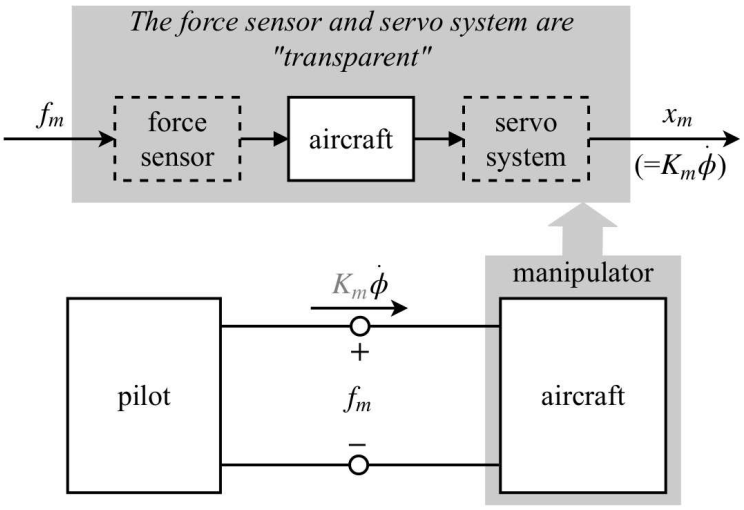

Fig. 12 Two-port representation [22, 23] of the pilot-manipulator system.

Then, independent of the aircraft dynamics, the *effective* dynamics of the controlled element now become a single integrator:

$$H_{c,eff} = \frac{\Phi(s)}{X_m(s)} = \frac{1}{K_m} \cdot \frac{1}{s} \tag{12}$$

The observed improvement related to target following can therefore be explained by the simplification of the controlled element. Moreover, it is readily appreciable that the disturbance to the aircraft becomes the disturbance to the manipulator. Rejection of the disturbance can then be easily achieved by stabilizing the manipulator position. Therefore, this task is integrated into the neuromuscular system, and becomes largely independent of the elimination of the visual error e. This explains the distinction in the response between target following and disturbance rejection.

In order to understand the effect of the forcing-function bandwidth on disturbance rejection, the impedance of the neuromuscular system of our subjects is estimated. Here, the term 'impedance' is a measure of how much the arm resists a disturbance motion. To this end, the pilot dynamics are first represented by three components, as shown by Fig. 13.

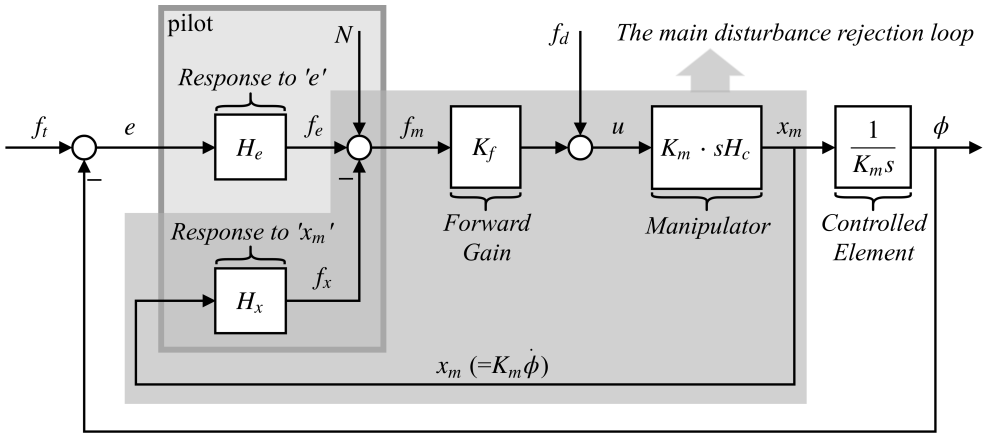

Fig. 13 The schematic diagram where the pilot is represented by to subsystems.

The pilot force f_m is divided into three components, i.e., f_x, f_e and N. The first two variables are the outputs of two internal systems H_x and H_e, and the last one accounts for the nonlinearity of the pilot dynamics. Assume for the moment that this remnant N is small as compared to f_e and f_x, then the dynamics of the pilot can be accurately described by two internal systems. The system H_x generates the force component in response to the movement of

Downloaded by TU DELFT on May 28, 2019 | http://arc.aiaa.org | DOI: 10.2514/6.2019-1231

the manipulator, and indicates the mechanical impedance of the neuromuscular system [20]. Due to the fact that the energy of the error signal e can be considered to be small at the frequencies of the disturbance (see Fig. 7b), disturbance rejection is mainly accomplished by the loop that is shaded in Fig. 13. In this case, the neuromuscular impedance H_x becomes the dynamic gain of the feedback path. This indicates that a greater magnitude of H_x will lead to better rejection of the disturbance.

The remainder of the pilot dynamics, including the pilot adaptation behavior, the internal representation, the neural filters and so forth [20], is accounted for by H_e. This system, which generates the force in response to the visually presented error signal, is used as an intermediate variable for separating H_x from the dynamics of the pilot. Readers are referred to the work by van Paassen et al. [20, 24] for greater detail about these two internal systems.

Fig. 14 shows the bode plot of H_x. In general, the phase characteristics corresponding to the three bandwidths are similar. However, higher forcing-function bandwidths lead to higher magnitudes of the impedance ($|H_x|$). This indicates that our subjects stiffened their arms when the disturbance on the manipulator became stronger. This is indeed confirmed by an interview carried out after the experiment with subjects.

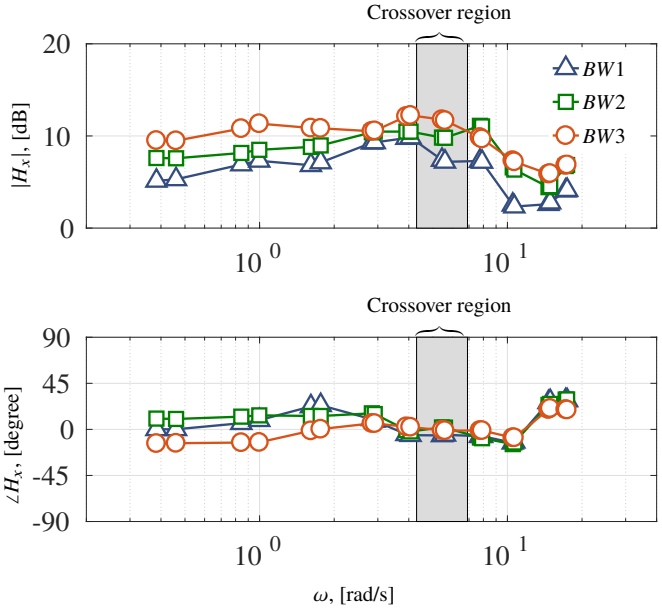

Fig. 14 The impedance of the neuromuscular system corresponding to the three forcing-function bandwidths.

The characteristics of H_x in the crossover region are consistent with the findings shown earlier (see Fig. 11). In the crossover region, the increase in $|H_x|$ increases the open-loop gain. As a result, the crossover frequency ω_c increases as the forcing-function bandwidth increases. The phase lags $\angle H_x$ corresponding to the three bandwidths are approximately the same. Therefore no significant changes in the phase margin ϕ_m were found.

VI. Haptic perception

As discussed above, the active manipulator reflects the dynamics of the controlled system. This allows the pilot to directly perceive the aircraft dynamics through the arm. An issue that was not explored in previous research with the active manipulator was the haptic perception of the controlled system's dynamics through the manipulator. One can imagine that the pilot's haptic perception of the active manipulator is different from perceiving the passive manipulator. Apart from the task performance, the dynamics of the active manipulator as perceived by the pilot is also an important factor in the design of a control system with an active manipulator. By drawing an analogy with basic mechanical properties, in this section we discuss the characteristics of the haptic perception of the active manipulator.

A. Haptic perception framework

The framework developed in our previous work [11, 16] will be used for the assessment of the haptic perception. To make this paper self-contained, we will first briefly summarize the main principle of this framework.

Downloaded by TU DELFT on May 28, 2019 | http://arc.aiaa.org | DOI: 10.2514/6.2019-1231

While haptically interacting with a dynamic system, humans develop their impressions of the system, depending on how the system behaves. Consider an operator interacting with an arbitrary dynamic system, as illustrated in Fig. 15, where f and x denote the force and displacement, respectively. Again, please note that the arrow under x indicates the direction of the energy flow which is not necessarily the same as the actual direction of the transmission of x [23].

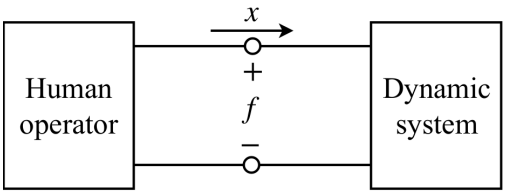

Fig. 15 Two-port representation of the system in which a human operator interacts with an arbitrary dynamic system [22].

We found that humans relate the behavior of a dynamic system to three basic mechanical properties, i.e., stiffness, damping and inertia (or mass) [11, 12, 25, 26]. In other words, humans are inclined to perceive the dynamic system with which they are interacting using their arm as having stiffness, damping and inertia properties, independently of the actual dynamics of the system. The perception related to these mechanical properties is determined by the correlation between the perceived movement x and force f. Although these two variables are perceived simultaneously, humans usually consider the movement to be the "cause" and the force to be the "effect", independently of the actual causality of the dynamic system [11–13]. The force against a *displacement* (spring force) is usually perceived as the behavior of a spring, the force resisting the *movement velocity* (viscous force) is identified with the effect of damping, and the effort to *change the movement direction* (inertia force) is related to inertia.

Therefore, human haptic perception of a dynamic system can be measured by means of these three mechanical properties. Now assume a linear dynamic system, and define G_{ds} as the system dynamics perceived by the human operator. In view of the causality used by humans, we define G_{ds} as the dynamics that correspond to the force in response to the displacement. The aforementioned correlation between the movement and force can be characterized by the frequency response function (FRF):

$$G_{ds}(\omega) = \frac{F(\omega)}{X(\omega)} = \Re G_{ds}(\omega) + \Im G_{ds}(\omega) \cdot j\,, \tag{13}$$

where F and X denote the Fourier transforms of the force f and the displacement x, respectively.

The characteristics of the FRF at each frequency indicate what the system will be perceived like when the human operator moves the system at this particular frequency. Since $G_{ds}(\omega)$ is a complex-valued function, it can be expressed with a real part $\Re G_{ds}$ and an imaginary part $\Im G_{ds}$. These two parts separate the correlation between the perceived movement and force into "two" components that are perpendicular in the complex plane.

The real part $\Re G_{ds}$ reflects the coupled correlations that humans use to estimate stiffness and inertia. This variable affects the perceived spring or inertia behavior, depending on the frequency of excitation [27]. When the system is moved at frequencies where $\Re G_{ds}$ is positive, it feels like a mechanical spring. In this case, the system generates a spring force of which the ratio to the displacement is $\Re G_{ds}$. When the system is excited at frequencies where $\Re G_{ds}$ is negative, it exhibits an inertia-like behavior. The system generates a force which is 180-degree out of phase with the displacement, thus directly proportional to the acceleration. Therefore, the sign of $\Re G_{ds}$ at the excitation frequencies determines which of these two mechanical behavior the system exhibits, and the magnitude of $\Re G_{ds}$ determines the amount of the corresponding force that a human operator perceives. The imaginary part $\Im G_{ds}$ determines the velocity-dependent force which humans relate to damping. The magnitude of it indicates the amount of the perceived damping force generated in response to a movement.

Therefore, what the dynamic system is perceived like can be derived from the characteristics of the complex valued FRF. A Nyquist plot of the FRF can offer an intuitive presentation of the characteristics of the haptic perception at different frequencies of excitation. Consider a typical mass-spring-damper system as an example. Its dynamics

Downloaded by TU DELFT on May 28, 2019 | http://arc.aiaa.org | DOI: 10.2514/6.2019-1231

corresponding to the human causality explained above can be expressed as:

$$\begin{aligned} G_{msd}(\omega) &= m \cdot (\omega j)^2 + b \cdot \omega j + k \\ &= \underbrace{k - m \cdot \omega^2}_{\Re G_{msd}(\omega)} + \underbrace{b \cdot \omega}_{\Im G_{msd}(\omega)} \cdot j \end{aligned} \tag{14}$$

This equation shows explicitly how the dynamics will be perceived in terms of the mass, spring and damper properties. Yet, it is still necessary for the introduction of the analysis based on the Nyquist plot.

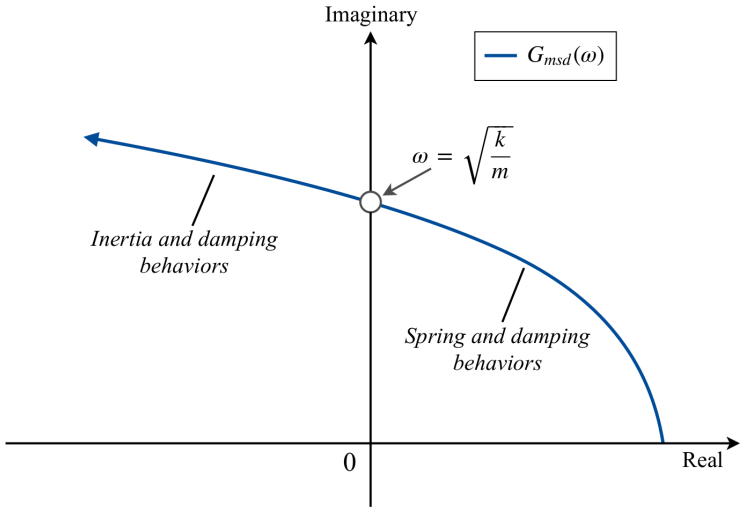

Fig. 16 Nyquist plot of a mass-spring-damper system $G_{msd}(\omega)$ (the dynamics corresponding to the human causality). The blue arrow indicates an increase in movement frequency.

Fig. 16 presents the Nyquist plot of this system. Each point of the curve represents the frequency response of the system at a particular frequency. As can be seen, the system generates mostly spring and damping forces when the human operator moves it at relatively low frequencies (the first quadrant where $\Re G_{msd} > 0$). It exhibits mostly inertia and damping forces when excited at higher frequencies (the second quadrant where $\Re G_{msd} < 0$). For this particular case, the frequency at which the sign of $\Re G_{msd}$ changes is the undamped eigen frequency ($\sqrt{\frac{k}{m}}$).

Therefore, the characteristics of the haptic perception of a dynamic system can be interpreted straightforwardly with the Nyquist plot. However, a system with a higher order may exhibit forces that correspond to different mass-spring-damper coefficients at different frequencies. To quantify the haptic perception for such cases, the concept of "effective impedance" can be adopted [28]. The principle of this concept is to match the FRF of the dynamic system at each frequency using the three isolated mechanical properties. However, one can imagine that the effective impedance varies with the frequency and does not provide straightforward information about the overall perception of the system.

Nevertheless, if the behavior of a system exhibited in response to manual excitation is still governed by a small number of dominant poles, the haptic perception of this system can still be accurately approximated with a mass-spring-damper system [11, 16, 28, 29]. This involves estimating the three mechanical properties of the mass-spring-damper system of which the FRF approximates to the FRF of the dynamic system. In the following section, we will assess the haptic perception of the active manipulator with our framework and attempt to quantify the perception using this method.

B. Haptic perception of the active manipulator

The assessment of the haptic perception of the active manipulator requires the FRF of its deflection-to-force dynamics. Again, we assume that the sampling and servo system have negligible effects on the overall dynamics in the frequency range of manual excitation. In addition, we leave the disturbance out of the investigation, as this external source does not change the manipulator dynamics. Thus, the perceived manipulator dynamics can be expressed as:

$$G_m(\omega) = \frac{F_m(\omega)}{X_m(\omega)} = \frac{u(\omega)}{K_m \Phi(\omega) \cdot \omega j} = \frac{1}{K_m} \cdot \frac{1}{H_c(\omega)\omega j} \tag{15}$$

Downloaded by TU DELFT on May 28, 2019 | http://arc.aiaa.org | DOI: 10.2514/6.2019-1231

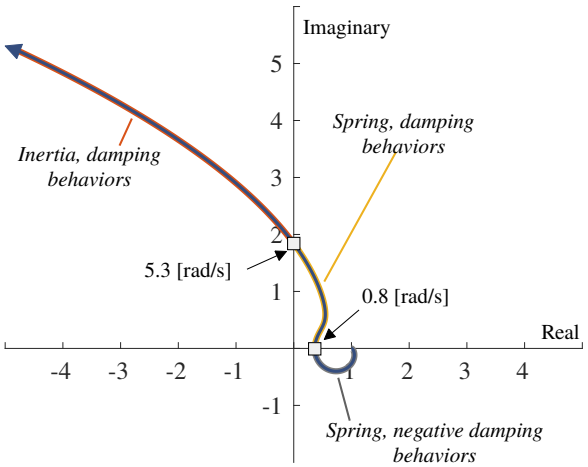

Fig. 17 Nyquist plot of the perceived dynamics of the active manipulator, for the frequency of 0 to 15 [rad/s].

Fig. 17 shows the Nyquist plot of the perceived manipulator dynamics G_m. The frequency range for this plot is 0 to 15 [rad/s]. The frequencies beyond this range are of no interest, as humans seldom intendedly generate such high-frequency movements in manual control tasks. As can be seen, the active manipulator in general possesses mass-spring-damper characteristics, despite the fact that it exhibits some negative damping behavior at frequencies below 0.8 [rad/s]. This is due to the partial cancellation of the two second-order polynomials in the numerator and the denominator of the aircraft dynamics (see Eq. (1)). Be that as it may, this unstable force only exists in a narrow range of fairly low frequencies, and its magnitude is considerably small. None of our subjects noticed this unstable behavior during the experiment.

The pilot will perceive the manipulator as having spring and damping properties in the frequency range between 0.8 to 5.3 [rad/s], and inertia and damping properties at higher frequencies. Moreover, the characteristics of the curve closely resemble that of a mass-spring-damper system (see Fig. 16). This allows us to quantify the haptic perception using the approximation approach mentioned earlier. This approximation involves the minimization of the difference in FRF between the dynamics given by Eq. (14) and the dynamics of the manipulator in the frequency range of interest:

$$J = \int_{\omega_0}^{\omega_1} \left| G_{msd}(i) - G_m(i) \right|^2 d\omega \tag{16}$$

As stated earlier, the frequency range is chosen as ω_0=0 to ω_1=15 [rad/s] ($\omega_0 = 0$, $\omega_1 = 15$).

Table 5 Estimates of the mechanical properties perceived from the active manipulator

m	b	k
[kgm^2]	[Nms/rad]	[Nm/rad]
0.0243	0.3489	0.6738

Table 5 lists the estimates of the perceived mechanical properties. The FRF of this mass-spring-damper system is shown in Fig. 18, along with the FRF of the manipulator. As can be seen, the only difference between the two systems lies in a narrow range of low frequencies. One can imagine that within this low-frequency range the actual perceived stiffness and damping properties will slightly deviate from the approximation. Apart from this minor difference, these two systems are nearly identical in FRF at most frequencies in the chosen frequency range. This indicates that the haptic perception of the active manipulator can be accurately characterized by the mechanical properties given in Table 5.

The active manipulator will be perceived the *same* as a passive manipulator. The aircraft dynamics considered in this study result in fairly good mass-spring-damper characteristics. In practice, although the aircraft dynamics are nonlinear, the behavior of an aircraft can still be approximated or is at least similar to the linear model derived from the equilibrium condition. Therefore the pilot's perception of the active manipulator will still be associated with similar mass-spring-damper characteristics.

Downloaded by TU DELFT on May 28, 2019 | http://arc.aiaa.org | DOI: 10.2514/6.2019-1231

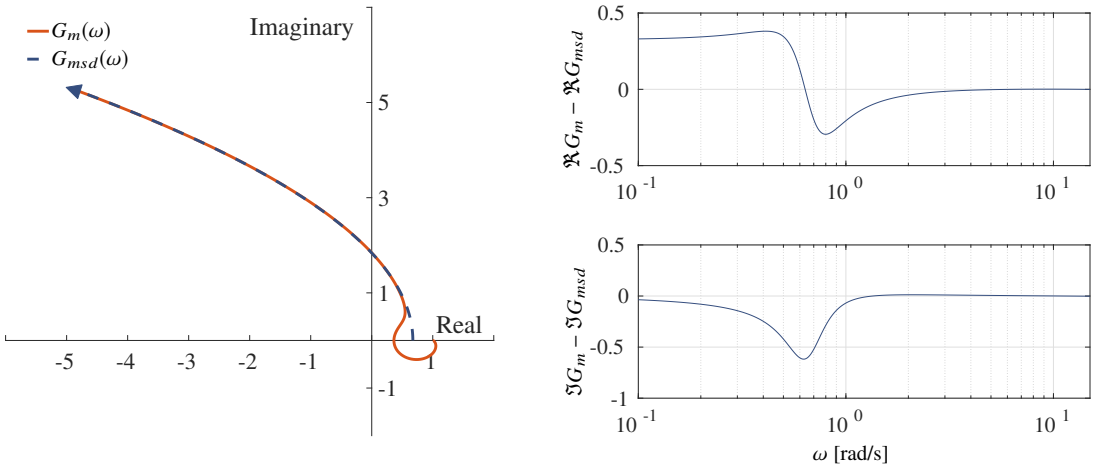

(a) Nyquist plot of G_{msd} and G_m

(b) Approximation error

Fig. 18 The approximate perception of the active manipulator.

Downloaded by TU DELFT on May 28, 2019 | http://arc.aiaa.org | DOI: 10.2514/6.2019-1231

VII. Discussion

In this study, we first revisited the active manipulator proposed in previous work [8, 9]. The observed improvement in the task performance is similar to the previous findings, except that in the previous work the effect of the manipulator type on the disturbance-rejection phase margin was not significant. However, this is probably due to the fact that the forcing functions used in our current work are different. As discussed in Section IV, the difference in ϕ_m between the two manipulator types may vary with different forcing-function bandwidths (see Fig. 11). Another possible reason lies in the number of subjects. In the previous work, only two subjects participated in the experiment, which may not be sufficient for the elimination of individual variations. In our current work, 12 subjects were invited, which would lead to a more generalized and reliable conclusion.

In addition, in the current study we evaluated the active manipulator with different forcing-function bandwidths, and revealed the reason for the improvement related to the active manipulator. In general, the active manipulator leads to a more pronounced improvement as the difficulty of the task increases. As discussed earlier, this is due to the fact that the active manipulator simplifies the dynamics of the controlled element into a single integrator, independently of the aircraft dynamics. Furthermore, with the active manipulator, the rejection of the disturbance is integrated into the *coupled* neuromuscular-manipulator system. This allows one to perform the disturbance-rejection task *separately* from the target-following task, and leads to a significant improvement.

As a result, the tasks of target following and disturbance rejection are largely allocated to the cerebellum which is responsible for the control of limb movements [30, 31]. The workload of the cerebrum, which is responsible for the equalization, is therefore reduced. This is quite distinct from the case of a passive manipulator, where the elimination of the error caused by both two forcing functions are mainly related to the cerebrum.

Furthermore, we also evaluated the active manipulator in terms of how its dynamics are perceived by the pilot. Using recent advances made in the understanding of human haptic perception, we revealed the characteristics of the perceived manipulator dynamics and quantified the perception with three basic mechanical properties. In general, the dynamics of most aircraft, when presented through the active manipulator, will exhibit behaviors with mass-spring-damper characteristics. This makes the active manipulator be perceived the same as a passive manipulator, but with possibly time-varying mass, spring, damper properties. That is, the perceived mechanical properties of the active manipulator also vary with the condition of the flight, which informs the pilot about the current flight condition, possibly enhancing situation awareness.

This study, in line with previous studies into active manipulators, used un-augmented aircraft dynamics. However, there is no reason why an active manipulator cannot be combined with an aircraft equipped with a stability augmentation system, given that one evaluates the effective dynamics of the manipulator to be compatible with control by the neuromuscular system. An additional advantage of such a set-up would be that pilots could also feel – through the manipulator – the effect of any flight envelope protection systems, or the actions of the autopilot. The current study

only evaluated the feedback of aircraft attitude rate on the stick. Rate feedback is a sensible choice, since it makes the dynamics controlled effectively those of a single integrator, which is known to result in high performance and low workload. Furthermore, a filtered feedback system could also be appropriate, creating further possibilities for optimizing the compatibility of the effective manipulator dynamics.

VIII. Conclusion

This study presents a new evaluation of a haptic interface for aircraft control. The proposed haptic interface, termed the active manipulator, feeds back the aircraft rotational velocity through the manipulator defection angle. Results from a first experiment indicated that the active manipulator led to a significant improvement in the task performance, as compared to the passive manipulator. We found that the active manipulator simplified the dynamics of the controlled element into a single integrator, independent of the actual aircraft dynamics. We also found that the disturbance rejection was integrated into the neuromuscular system, and became largely independent of the target following task. Furthermore, the active manipulator was evaluated in terms of what it would be perceived as. Using the result from the work on haptic perception, we demonstrated that the pilot's haptic perception of the active manipulator can be well characterized, and quantified, by using three basic mechanical properties (stiffness, damping and inertia).

Downloaded by TU DELFT on May 28, 2019 | http://arc.aiaa.org | DOI: 10.2514/6.2019-1231

References

[1] Ferrell, W. R., "Delayed Force Feedback," *Human Factors*, Vol. 8, No. 5, 1966, pp. 449–455.

[2] Anderson, R. J., and Spong, M. W., "Bilateral Control of Teleoperators with Time Delay," *IEEE Trans. on Automatic Control*, Vol. 34, No. 5, 1989, pp. 494–501.

[3] Niemeyer, G., and Slotine, J. J., "Stable Adaptive Teleoperation," *IEEE J. of Oceanic Engineering*, Vol. 16, No. 1, 1991, pp. 152–162.

[4] Ryu, J. H., Kwon, D. S., and Hannaford, B., "Stable Teleoperation with Time-domain Passivity Control," *IEEE Trans. on Robotics and Automation*, Vol. 20, No. 2, 2004, pp. 365–373.

[5] Hirche, S., Matiakis, T., and Buss, M., "A Distributed Controller Approach for Delay-independent Stability of Networked Control Systems," *Automatica*, Vol. 45, No. 8, 2009, pp. 1828–1836.

[6] De Stigter, S., Mulder, M., and van Paassen, M. M., "Design and Evaluation of a Haptic Flight Director," *J. of Guidance, Control, and Dynamics*, Vol. 30, No. 1, 2007, pp. 35–46.

[7] Mulder, M., Abbink, D. A., van Paassen, M. M., and Mulder, M., "Design of a Haptic Gas Pedal for Active Car-following Support," *IEEE Trans. on Intelligent Transportation Systems*, Vol. 12, No. 1, 2011, pp. 268–279.

[8] Hosman, R. J. A. W., Benard, B., and Fourquet, H., "Active and Passive Side Stick Controllers in Manual Aircraft Control," *1990 IEEE Int. Conf. on Systems, Man and Cybernetics (SMC)*, Los Angeles, USA, 1990, pp. 527–529.

[9] Hosman, R. J. A. W., and Van der Vaart, J. C., "Active and Passive Side Stick Controllers: Tracking Task Performance and Pilot Control Behavior," *AGARD Conf. on the Man-Machine Interface in Tactical Aircraft Design and Combat Automation*, Vol. AGARD-C8-424, Stuttgart, Germany, 1988, pp. 26–1 – 26–11.

[10] Adams, R. J., and Hannaford, B., "Stable Haptic Interaction with Birtual Environments," *IEEE Trans. Robotics and Automation*, Vol. 15, No. 3, 1999, pp. 465–474.

[11] Fu, W., van Paassen, M. M., Abbink, D. A., and Mulder, M., "Framework for Human Haptic Perception with Delayed Force Feedback," *IEEE Trans. on Human-Machine Systems*, under review.

[12] Fu, W., Landman, A., van Paassen, M. M., and Mulder, M., "Modeling Human Difference Threshold in Perceiving Mechanical Properties from Force," *IEEE Trans. Human-Machine Systems*, Vol. 48, No. 4, 2018, pp. 359–368.

[13] Fu, W., van Paassen, M. M., and Mulder, M., "On the Relationship Between the Force JND and the Stiffness JND in Haptic Perception," *ACM Symp. on Applied Perception*, ACM, Cottbus, Germany, 2017.

[14] Fu, W., van Paassen, M. M., Stroosma, O., and Mulder, M., "Objective Inceptor Cueing Test for Control Loading Systems: Principle and Initial Design," *AIAA Modeling and Simulation Technologies Conf.*, Denver, USA, 2017.

[15] Fu, W., van Paassen, M. M., and Mulder, M., "The Influence of Discrimination Strategy on the JND in Human Haptic Perception of Manipulator Stiffness," *AIAA Modeling and Simulation Technologies Conf.*, Denver, USA, 2017.

[16] Fu, W., van Paassen, M. M., and Mulder, M., "Perception Centered Transparency Evaluation of Wave-variable based Bilateral Teleoperation," *2018 IEEE Int. Conf. on Systems, Man and Cybernetics (SMC)*, Miyazaki, Japan, 2018.

[17] Fu, W., van Paassen, M. M., and Mulder, M., "Modeling the Coupled Difference Threshold of Perceiving Mass and Stiffness from Force," *2018 IEEE Int. Conf. on Systems, Man and Cybernetics (SMC)*, Miyazaki, Japan, 2018.

[18] Heffley, R. K., and Jewell, W. F., "Aircraft Handling Qualities Data," Tech. rep., NASA, December 1972.

[19] van Paassen, M. M., and Mulder, M., "Identification of Human Control Behavior," *Int. Encyclopedia of Ergonomics and Human Factors (2nd Edition)*, edited by W. Karwowski, Taylor & Francis, London, UK, 2006, pp. 400–407.

[20] van Paassen, M. M., Van Der Vaart, J. C., and Mulder, J. A., "Model of the Neuromuscular Dynamics of the Human Pilot's Arm," *J. of Aircraft*, Vol. 41, No. 6, 2004, pp. 1482–1490.

[21] McRuer, D. T., and Jex, H. R., "A Review of Quasi-linear Pilot Models," *IEEE Trans. on Human Factors in Electronics*, , No. 3, 1967, pp. 231–249.

[22] Hannaford, B., "A Design Framework for Teleoperators with Kinesthetic Feedback," *IEEE Trans. on Robotics and Automation*, Vol. 5, No. 4, 1989, pp. 426–434.

[23] Haykin, S. S., *Active Network Theory*, Vol. 2680, Addison-Wesley, 1970.

[24] van Paassen, M. M., "Biophysics in Aircraft Control: A Model of the Neuromuscular System of the Pilot's Arm," Ph.D. thesis, TU Delft, Delft University of Technology, 1994.

[25] Pressman, A., Welty, L. J., Karniel, A., and Mussa-Ivaldi, F. A., "Perception of Delayed Stiffness," *The Int. J. of Robotics Research*, Vol. 26, No. 11-12, 2007, pp. 1191–1203.

[26] Nisky, I., Mussa-Ivaldi, F. A., and Karniel, A., "Analytical Study of Perceptual and Motor Transparency in Bilateral Teleoperation," *IEEE Trans. on Human-Machine Systems*, Vol. 43, No. 6, 2013, pp. 570–582.

[27] Findeisen, D., *System Dynamics and Mechanical Vibrations: An Introduction*, Springer Science & Business Media, 2013.

[28] Colonnese, N., Siu, A. F., Abbott, C. M., and Okamura, A. M., "Rendered and Characterized Closed-loop Accuracy of Impedance-type Haptic Displays," *IEEE Trans. on Haptics*, Vol. 8, No. 4, 2015, pp. 434–446.

[29] Schauß, T., and Peer, A., "Parameter-space Transparency Analysis of Teleoperation Systems," *2012 IEEE Haptics Symp. (HAPTICS)*, 2012, pp. 111–116.

[30] Wolpert, D. M., and Ghahramani, Z., "Computational Principles of Movement Neuroscience," *Nature Neuroscience*, Vol. 3, 2000, pp. 1212–1217.

[31] Kawato, M., "Internal Models for Motor Control and Trajectory Planning," *Current Opinion in Neurobiology*, Vol. 9, No. 6, 1999, pp. 718–727.

Downloaded by TU DELFT on May 28, 2019 | http://arc.aiaa.org | DOI: 10.2514/6.2019-1231